

Excited State Potentials and Ligand Force Field of a Blue Copper Protein Plastocyanin

Koji Ando[†]

School of Chemistry, University of Birmingham, Edgbaston, Birmingham B15 2TT, United Kingdom

Received: November 10, 2003; In Final Form: January 6, 2004

The ground and excited state potentials and force field of the copper ion site of plastocyanin in the oxidized state is studied by ab initio electronic structure calculations, with the aim to explore the mechanism of its photodynamics. It is shown that the potential energy surface of the ligand-to-metal charge-transfer (LMCT) state, which corresponds to the intense ~ 600 nm absorption, is repulsive along the Cu–S(Cys) distance, where S(Cys) denotes the sulfur atom of the cysteine ligand, and crosses with the $d \rightarrow d$ ligand field excited states at the Cu–S(Cys) length of ~ 2.7 Å or longer. The crossing distance varies depending on the Cu–N(His) distance of the two histidine ligands, indicating that the Cu–His ligand vibrational motions, in addition to the Cu–S(Cys) stretch, constitute a major component of the reaction coordinate for the nonradiative transitions. This feature is explained in terms of the different charge distributions and the resulting electrostatic interactions in these states. The influence from the methionine ligand is seen to be minor, although the possible dynamical coupling via the dispersion interactions is not ruled out. A shorter Cu–S(Met) equilibrium distance (2.4 Å) than in the crystal structure (2.9 Å) is found, suggesting that the structural constraint from the surrounding protein may be playing some role.

1. Introduction

Plastocyanin is a type I blue copper protein involved in photosynthesis in higher plants and algae as an electron carrier.^{1,2} X-ray diffraction crystallography^{3,4} has revealed a distorted trigonal ligand structure around the copper ion formed by a cysteine (Cys) and two histidine (His) residues. A fourth ligand of methionine (Met) is also found in the axial direction of the trigonal plane at a longer distance than is expected for a stable ligand complex. The solution structure has been also investigated by proton NMR spectroscopies.⁵

The optical absorption spectra of plastocyanin in oxidized state show broad peaks at around 600 and 770 nm, which have been assigned as a S(Cys) \rightarrow Cu ligand-to-metal charge-transfer (LMCT) transition and $d \rightarrow d$ ligand field (LF) transitions, respectively.⁶ Resonance Raman spectra indicate that several ligand vibrational motions, such as Cu–Cys and Cu–His modes, are induced by photoexcitation to the LMCT state.⁷

More recently, time-resolved pump–probe measurements have been carried out to study the ultrafast response of plastocyanin^{8–10} and proposed that the LMCT state decays to the ground state via populating the $d \rightarrow d$ state in the time scales of a few hundred femtoseconds. The time-resolved signal accompanies coherent oscillations coming from the environmental vibrations, which should contain rich information on the energetic and dynamical coupling of the protein to the charge-transfer processes. The study of the photodynamics is thus expected to provide insights into the mechanism of the physiological redox electron transfers.

Quantum mechanical electronic structure calculations have been playing a vital role in the interpretation of the observed optical properties. To date, calculations at various levels, from the semiempirical $X\alpha$ ⁶ and CNDO/S¹¹ to the most recent DFT¹² and ab initio CASPT2,^{13,14} have been reported. These works

are primarily focused on the static properties around the equilibrium structure of the active site models. It would be thus intriguing to proceed to examine the electronic properties in conjunction with the photodynamics, with the aim to elucidate the detailed microscopic mechanism of the time-resolved spectra.

In this work, we carry out ab initio quantum mechanical calculations to construct potential energy functions and force fields of the plastocyanin active site. Although an extensive molecular dynamics (MD) simulation analysis^{15–18} is to be reported in the forthcoming publications, the results at this stage are substantially suggestive of new insights into the microscopic mechanism of the plastocyanin photodynamics.

2. Computational

Copper Site Model and Structure. The amino acid ligands around the Cu(II) ion of plastocyanin is modeled by replacing the cysteine by SCH_3^- , methionine by $\text{S}(\text{CH}_3)_2$, and histidine by $\text{Im}=\text{C}_3\text{H}_4\text{N}_2$ where Im denotes the imidazole ring. The structure of this truncated amino acid model, $\text{Cu}(\text{SCH}_3)(\text{Im})_2\text{--}(\text{S}(\text{CH}_3)_2)^+$, is shown in Figure 1.¹⁹ The coordinates of the atoms other than hydrogen are taken from the Protein Data Bank (1bxu.pdb) and have been determined by X-ray crystallography on *Synechococcus* sp. PCC 7942 plastocyanin.⁴ The coordinates of the hydrogen atoms are determined by a geometry optimization with the semiempirical PM3 Hamiltonian,²⁰ in which the coordinates of all the heavy atoms are fixed. [Due to the unavailability of well-established semiempirical parameters for copper, we replaced the copper atom by zinc, assuming that it will not affect the hydrogen positions.]

Ligand Field Atomic Charges. The ab initio restricted open-shell Hartree–Fock (ROHF) method²¹ and Kohn–Sham density functional theory (KS-DFT) with B3LYP functionals^{22–24} are employed to calculate the electronic energy and density of the $\text{Cu}(\text{SCH}_3)(\text{Im})_2(\text{S}(\text{CH}_3)_2)^+$ model. The 6-31G* basis set^{25–27} is

[†] E-mail: K.Ando@bham.ac.uk.

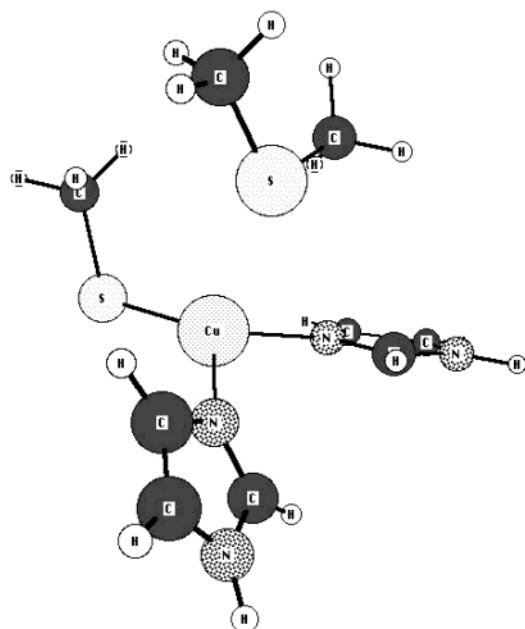


Figure 1. Copper ion site of plastocyanin with the truncated amino acid models of Cys, Met and two His ligands, $\text{Cu}(\text{SCH}_3)(\text{Im})_2(\text{S}(\text{CH}_3)_2)^+$. [In the Im ring, N_δ ligates to the copper, C_ϵ is bonded between the two nitrogen atoms, and C_γ is the other carbon bonded to N_δ .] The coordinates of the hydrogen atoms were optimized by ROHF/PM3 calculation, with the heavy atoms fixed at the crystal structure (1bxu.pdb), where $\text{Cu}-\text{S}(\text{Cys}) = 2.14 \text{ \AA}$, $\text{Cu}-\text{S}(\text{Met}) = 2.94 \text{ \AA}$, and $\text{Cu}-\text{N}_\delta(\text{His}) = 1.97$ and 2.01 \AA with the resolution of 1.9 \AA .

used throughout. The exponents of the f-type Gaussian basis functions on copper and d-type functions on sulfur are 0.8 and 0.65, respectively. The number of basis functions is 306. These calculations are to obtain the effective point charges listed in Tables 1 and S1. The KS-DFT method is also used to obtain Figure 10.

PDCNP: Potential Derived Charges Restrained around the Natural Populations. The potential derived charges (PDC) provide a sound description of the atomic charges for use in molecular simulations. The atomic charges are determined via the least-squares fitting procedure to minimize

$$\chi^2 = \sum_i^{N_v} (V_i - v_i)^2 \quad (1)$$

where V_i is the target electrostatic potential evaluated from the quantum mechanical calculations and v_i is calculated from the atomic charges (q_a) to be determined. The index i runs through a set of N_v space points promptly generated around the molecule.²⁸ The PDC results are often ill-determined for large polyatomic molecules in such a way that notably different charge sets can reproduce the target potentials equally well. The results may be thus dependent on the details of the procedure, e.g., the method to generate the points around the molecule.

In this work, we employ the figures of merit of a form

$$\chi^2 = w_v \sum_i^{N_v} (V_i - v_i)^2 + w_q \sum_a^{N_q} (q_a - Q_a)^2 \quad (2)$$

where Q_a are the charges from the natural population analysis (NPA),³⁷ N_q is the number of atomic charge sites, and w_v and w_q are the weight factors. This is in the same spirit as the RESP method²⁹ in which the Mulliken charges have been employed for the target charges. It is now well recognized that the NPA

charges are more robust against the variation of the size of the basis set. Another distinct feature here is the choice of the weights

$$w_v = \left(\sum_i^{N_v} V_i^2 \right)^{-1} \quad w_q = \left(\sum_a^{N_q} Q_a^2 \right)^{-1} \quad (3)$$

by which both the potential and charge terms in χ^2 are made dimensionless. Moreover, because these w_v and w_q are of the order N_v^{-1} and N_q^{-1} , respectively, the magnitudes of the two terms in χ^2 become insensitive to these size parameters, so we expect a balanced use of these terms that have distinct physical nature from each other.

Excited State Wave Functions and Potentials. On the basis of the results and discussion in section 3.1, we consider that the $\text{Cu}(\text{SCH}_3)^+$ moiety is the essential core to discuss the excited state dynamics, on which high level electron-correlated calculations are carried out. The $\text{S}(\text{CH}_3)_2$ and Im ligands are modeled by the effective point charges in Tables 1 and S1 to influence the core part $\text{Cu}(\text{SCH}_3)^+$ via the Coulomb interaction. We denote this kind of partition into the quantum and point charge models as $\text{Cu}(\text{SCH}_3)^+//(\text{S}(\text{CH}_3)_2)(\text{Im})_2$. The excited state wave functions are computed by the multiconfiguration self-consistent field (MCSCF) method with the occupation restricted multiple active spaces (ORMAS)³⁰ and the multiconfiguration quasi degenerate perturbation theory (MCQDPT)³¹ from the complete active space (CASSCF)³² wave function. In the ORMAS-MCSCF calculations, the active molecular orbitals (MOs) are divided into three subspaces, (1) five MOs from the copper 3d orbitals, (2) six valence MOs from the sulfur 3p σ and π lone pairs, $\text{Cu}-\text{S} \sigma^*$, $\text{Cu} 4p \pi^*$, and two $\text{Cu} 4p \sigma^*$ orbitals (the σ/π classification is with respect to the $\text{Cu}-\text{S}-\text{C}$ plane), and (3) five correlating $4d^*$ orbitals. Thirteen electrons are distributed in these subspaces, in which up to a single hole is allowed in the five 3d MOs, three or four electrons are fully distributed in the six valence MOs, and up to a single electron is allowed in the five $4d^*$ MOs. The number of the configuration state functions (CSFs) is then 9065. In the CASSCF-MCQDPT calculations, the second-order QDPT correction is evaluated from the state-averaged CASSCF wave function where 13 electrons are fully distributed in 10 active MOs composed of the subspaces 1 and 2 defined above but excluding one of the $4p \sigma^*$ MOs. The CASSCF wave function thus consists of 25 200 CSFs. In both the ORMAS-MCSCF and CASSCF calculations, the lowest seven states (in C_1 symmetry) are averaged with equal weight. The results are shown in Figures 2–5 and Tables 2 and 3.

Ligand Force Field Parameters. The interaction potentials between the core $\text{Cu}(\text{SCH}_3)^+$ part and the Im or $\text{S}(\text{CH}_3)_2$ ligands are calculated with models partitioned as $\text{Cu}(\text{SCH}_3)(\text{Im})^+//(\text{S}(\text{CH}_3)_2)(\text{Im})$ or $\text{Cu}(\text{SCH}_3)(\text{S}(\text{CH}_3)_2)^+//(\text{Im})_2$, respectively, at the second-order Moller–Plesset (MP2) level.³³ The Z-averaged perturbation theory (ZAPT)³⁴ from the ROHF wave function is employed. The results are shown in Figures 7–9.

All the electronic structure calculations were performed with the program GAMESS.³⁵ Other nonstandard computations and further details are described promptly in the following sections.

3. Results and Discussion

3.1. Atomic Charge Force Field of His and Met Ligands.

We begin with the ROHF and KS-DFT calculations on the $\text{Cu}(\text{SCH}_3)(\text{Im})_2(\text{S}(\text{CH}_3)_2)^+$ model. The primary aim is to determine the effective point charges (EPC) of the ligand atoms to be used in the subsequent calculations on the partitioned

TABLE 1: Atomic Charges in the $\text{Cu}(\text{SCH}_3)(\text{Im})_2(\text{S}(\text{CH}_3)_2)^+$ Model^a

residue	atom	B3LYP/6-31G*		
		Mulliken	NPA	PDCNP
Cys84	Cu	0.6415	1.2094	1.1947
	C _β	-0.5988	-0.8273	-0.8159
	S _γ	-0.1206	-0.3340	-0.3415
Met92	C _γ	-0.6011	-0.8219	-0.8179
	S _δ	0.0950	0.1701	0.1615
	C _ε	-0.6193	-0.8467	-0.8331
His37	C _γ	0.0213	-0.0793	-0.0908
	N _{δ1}	-0.5811	-0.6788	-0.6781
	C _{δ2}	0.0211	-0.0749	-0.0713
His87	C _{ε1}	0.2584	0.1974	0.1964
	N _{ε2}	-0.5496	-0.5329	-0.5225
	C _γ	0.0312	-0.0771	s.a.
	N _{δ1}	-0.5598	-0.6648	s.a.
	C _{δ2}	0.0253	-0.0682	s.a.
	C _{ε1}	0.2529	0.1960	s.a.
	N _{ε2}	-0.5457	-0.5332	s.a.

^a NPA = natural populations analysis. PDCNP = potential derived charges constrained around natural populations. s.a. = same as above for the same atom type.

TABLE 2: Excitation Energies (cm⁻¹) of the $\text{Cu}(\text{SCH}_3)^+//(\text{S}(\text{CH}_3)_2)(\text{Im})_2$ Model

state ← 0	with EPC ^a		without EPC		exp ^b
	MCQDPT	ORMAS	MCQDPT	ORMAS	
1	4660	8000	10390	9740	5000
2	13320	10560	17410	15220	10800
3	13660	10680	17680	15250	12800
4	14150	11630	17960	15710	13950
5	21660	20680	21580	16710	16700
6	26820	32447	26790	20350	21390

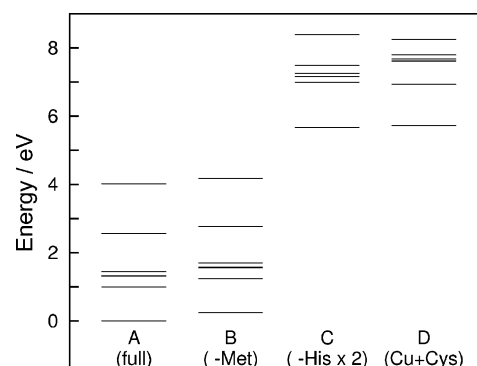
^a EPC = effective point charges of the ligand models. ^b References 6 and 14.

models such as $\text{Cu}(\text{SCH}_3)^+//(\text{S}(\text{CH}_3)_2)(\text{Im})_2$. The results are given in Tables 1 and S1, which include the standard Mulliken charges,³⁶ NPA and the PDCNP, described in section 2. Because the difference between the two His ligands³⁸ is found to be minor, their average is taken for the PDCNP results. It is seen that the charge on the N_δ(His) atom, which is ligated to the copper ion, is negative, suggesting stabilization of the ligand structure due to the Coulomb interaction. On the other hand, the S(Met) atom has a positive charge, which would be unfavorable in terms of the local charge-dipole interaction with the copper ion. Nonetheless, because of the softness of the thioether group, the dispersion interaction could be dominant in the Cu–Met interaction. This is further examined in section 3.3.

We have also carried out the natural bond orbital (NBO) analysis³⁷ from the ROHF and KS-DFT electron density matrices. The NBO analysis suggests a covalent Cu–S(Cys) bond with the occupancy of 1.98 from both the ROHF and KS-DFT calculations. On the other hand, the analysis suggests no bonding between Cu and His or Met ligands.

Considering that the DFT partially includes the electron-correlation effects that are missed in ROHF, we use the PDCNP charges from KS-DFT in the subsequent higher level calculations on the partitioned model.

3.2. Excited State Potential Energies of the Cu–Cys Complex. Table 2 lists the excitation energies from the ground to the lowest six excited states by the MCQDPT and ORMAS-MCSCF calculations on the $\text{Cu}(\text{SCH}_3)^+//(\text{S}(\text{CH}_3)_2)(\text{Im})_2$ model. Calculations without the effective point charges of the His and Met ligands are included for comparison. The excitation energies

**Figure 2.** Ground and excited state energy levels for (A) $\text{Cu}(\text{SCH}_3)^+//(\text{S}(\text{CH}_3)_2)(\text{Im})_2$ model with the Met and two His ligand fields, (B) $\text{Cu}(\text{SCH}_3)^+//(\text{Im})_2$, (C) $\text{Cu}(\text{SCH}_3)^+//(\text{S}(\text{CH}_3)_2)$, i.e., removed Met or two His from (A), respectively, and (D) bare $\text{Cu}(\text{SCH}_3)^+$.

to the first four states decrease by including the electrostatic interaction with the ligands. On the other hand, the excitation energies to the fifth and sixth states increase, though the quantitative amount of increase is notably smaller by MCQDPT. Overall, we consider that MCQDPT and ORMAS-MCSCF give comparable qualities, the former being slightly better, for the excitation energies, with the computational cost being much smaller for the latter. We hence employ ORMAS-MCSCF for the rest of the calculations in this subsection.

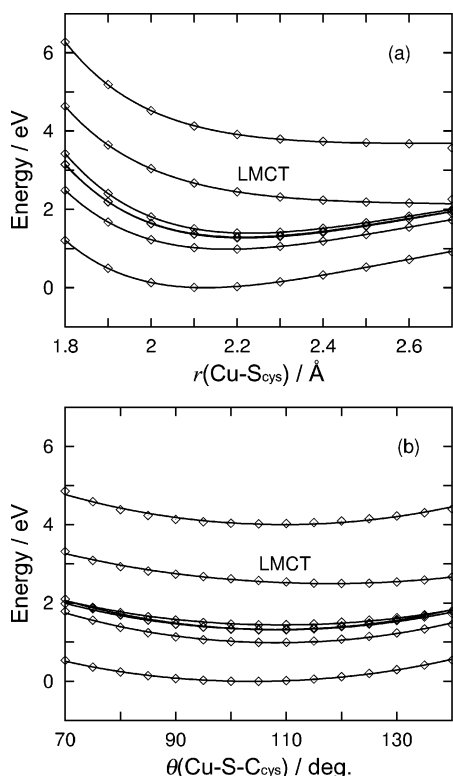
It would be appropriate here to comment on the partitioned model of $\text{Cu}(\text{SCH}_3)^+//(\text{S}(\text{CH}_3)_2)(\text{Im})_2$. The NBO analysis described in section 3.1 pertains to the ground state and does not exclude the possibility of the involvement of His and Met ligands in the excited states. Nonetheless, we refer to the previous CASPT2 calculations¹³ on larger model complexes, which demonstrated that the excitations to the lowest six states are mostly localized around the Cu–Cys part, and the His and Met ligands play passive “spectator” roles. This would be rationalized from the localized and contracted nature of the 3d orbitals (as in the rationale for the traditional ligand field theory). To further test this, we have carried out the ORMAS-MCSCF calculations including one of the His ligands into the quantum part and confirmed that the contributions from the His ligands are negligible in the dominant active MOs (see Supporting Information). We therefore consider that the major consequence of the present classical description of the ligands is the quantitative deviation of the excitation energies, as observed in Table 2, and that the present approximation would be adequate to obtain semiquantitatively accurate potential energy surfaces. [It would be possible and useful, if necessary, to introduce numerical corrections to the potential functions developed below for MD simulation analysis.]

Figure 2 shows alteration of the electronic energy levels caused by removal of the ligands. It is apparent that the two His ligands alter the energy levels most significantly, whereas the effect of the Met ligand is almost negligible. Table 3 shows the PDCNP charges from the ORMAS-MCSCF wave functions. It suggests that the fifth and sixth excited states (with EPC) have the LMCT character. The fifth state corresponds to the major optical absorption peak at ~600 nm. Further analysis on the CSFs indicates that the second, third, and fourth excited states are characterized by the $d \rightarrow d$ excitations (see Supporting Information), which we denote $d-d$ LF (ligand field) states.

The Cu charges in Table 3 suggest that the LMCT involves transfer of net charges of 0.44 unit. This number is twice as large as that suggested previously from the semiempirical X α calculation.⁶ We should note here that the charge transfer in

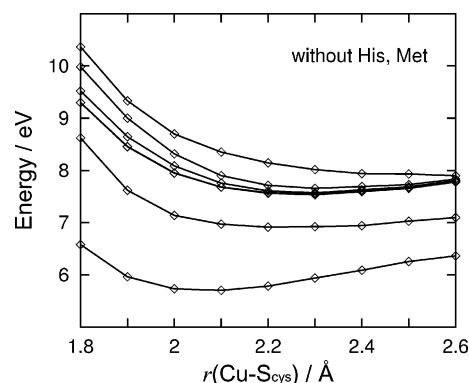
TABLE 3: Atomic Charges of the Cu(SCH₃)^{+/−}(S(CH₃)₂(Im)₂ Model

state	with EPC ^a			without EPC		
	Cu	S	C _β	Cu	S	C _β
0	1.491	−0.498	−0.786	1.041	−0.085	−0.820
1	1.548	−0.561	−0.779	1.107	−0.158	−0.810
2	1.561	−0.573	−0.777	1.218	−0.281	−0.799
3	1.560	−0.571	−0.778	1.224	−0.286	−0.799
4	1.574	−0.590	−0.774	1.227	−0.289	−0.799
5	1.058	−0.029	−0.822	1.205	−0.269	−0.800
6	0.891	0.157	−0.844	0.817	0.129	−0.834

^a EPC = effective point charges of the ligand models.**Figure 3.** Ground and excited state potential energies of the Cu(SCH₃)^{+/−}(S(CH₃)₂(Im)₂ model along (a) the Cu–S(Cys) distance and (b) the Cu–S–C(Cys) angle. The internal coordinates other than the varying ones are fixed at the initial geometry. The marked points are from the ORMAS-MCSCF calculations, and the solid curves are from the functional fit to eqs 4 and 5.

terms of the net atomic population is not a well-defined observable quantity but dependent on the computational definition. We find that the charge transfer from the conventional Mulliken analysis is slightly smaller, 0.40, but still larger than the X α suggestion. We consider that the PDCs are most relevant to the molecular interactions and therefore suited for the present purpose to develop potential functions and force fields for molecular simulations.

We have repeated the ORMAS-MCSCF calculations to construct the potential energy curves along the Cu–S distance and the Cu–S–C angle of Cu(SCH₃)⁺. The results are displayed in Figure 3. It is seen that the fifth and sixth excited states, of the LMCT character, are repulsive along the Cu–S distance whereas the other lower states have bound potential. This is to be compared with Figure 4, calculated without the His and Met ligand fields, which shows all the six excited states nearly repulsive or only weakly bound. It is also seen in Figure 4 that the second and third excited states are mostly degenerate in the entire coordinate range, and nearly degenerate with the fourth

**Figure 4.** Same as Figure 3a, but for the isolated Cu(SCH₃)⁺ system, i.e., without the ligand field point charges.

and fifth states. To these the sixth state also approaches along the Cu–S distance. The atomic charges in Table 3 indicate that the fifth state without the ligand field is not of LMCT character.

The assortment of the results so far suggests, in summary, that the ligand fields from His and Met, in particular the former, are essential for the LMCT character of the excited state that corresponds to the 600 nm absorption, in such a way that the electrostatic interaction separates the energy level of the LMCT state from the other states, including the d–d LF states, by stabilizing the latter more than the former. This is understood from the charge distribution analysis and their electrostatic interactions. The interpretation is further supported by table S2, which compares the Coulomb interactions between the Cu–Cys core part and the His and Met ligands computed from the atomic charges.

Figure 3b shows the potential energy curves along the Cu–S–C bending angle. The curves are nearly parallel, having the minima at 105–110°, except the fifth LMCT state whose minimum is shifted to the larger angle by ~20°. However, because the curvatures are small and the fifth state is well separated from the other states, the Cu–S–C bending motion does not seem to couple significantly to the nonradiative transitions.

Figure 5 plots the PDCNP charges for the representative states along the Cu–S and Cu–S–C internal coordinates. In both the LMCT and the d–d LF states the copper charge decreases along the Cu–S distance, along with the increase of the sulfur charge, whereas the carbon charge stays nearly constant. However, the quantitative variation is small, especially in the region of the Cu–S distance longer than the ground state equilibrium of ~2.1 Å, i.e., the region most relevant in the photodynamics. We thus employ fixed charges at the values in Table 3 for the construction of potential energy functions to be described now.

The solid curves in Figure 3 are from functional fittings of the discrete points of the ORMAS-MCSCF calculations. Along the Cu–S distance r , we employ

$$V(r) = V_{el}(r) + D(1 - e^{-a(r-r_e)})^2 + V_0 \quad (4)$$

where $V_{el}(r)$ is the Coulomb potential between the Cu–Cys complex and the other ligands computed from the atomic point charges of Tables 1 and 3. Namely, we first subtract $V_{el}(r)$ from the ORMAS-MCSCF energy and then fit the remainder to the Morse function. Along the Cu–S–C angle θ , we employ a simple harmonic form

$$V(\theta) = V_{el}(\theta) + K(\theta - \theta_e)^2 + V'_0 \quad (5)$$

The resultant parameters from the least-squares fittings are listed in Table S3.

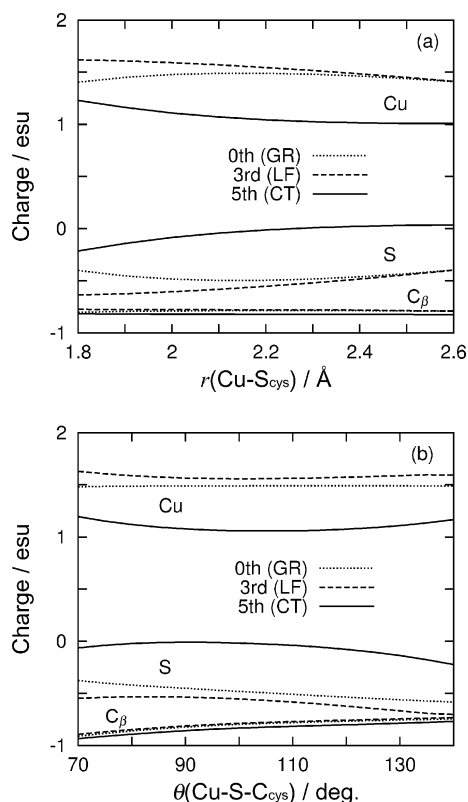


Figure 5. PDCNP atomic charges derived from the calculations in Figure 3. The solid, dashed, and dotted lines are for the fifth LMCT, third d-d LF excited states, and the ground state, respectively.

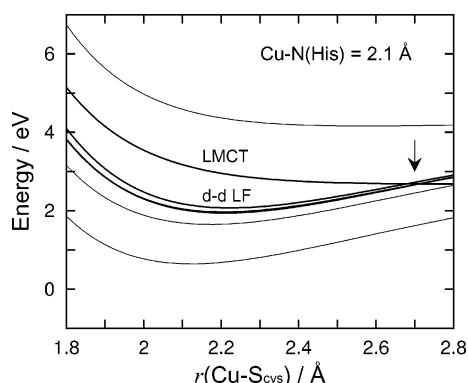


Figure 6. Diabatic model potentials along the Cu-S(Cys) distance evaluated at the Cu-N(His) distance of the two His ligands, both shifted to 2.1 Å.

The potential functions of the electronic states determined in this way would form approximate diabatic states useful to discuss the surface crossing and nonradiative transitions. Figure 6 shows how these diabatic curves are modified when the two His ligands are separated from the metal center. The calculation here includes the short-range interaction to be described in section 3.3. It is seen that the lower states including the d-d LF states are destabilized by separating the His ligands from the Cu ion, such that the diabatic surface crossing between the LMCT and d-d LF states now occurs at the Cu-S distance of ~ 2.7 Å. This behavior is explained in terms of the different electrostatic interaction between the states, in the same way as has been discussed above.³⁹ The analysis suggests that the metal-ligand vibrational motions of the His ligands constitute a major component of the reaction coordinate in the nonradiative transitions from the LMCT to d-d LF states in the plastocyanin photodynamics. The interaction between the Cu-Cys core and

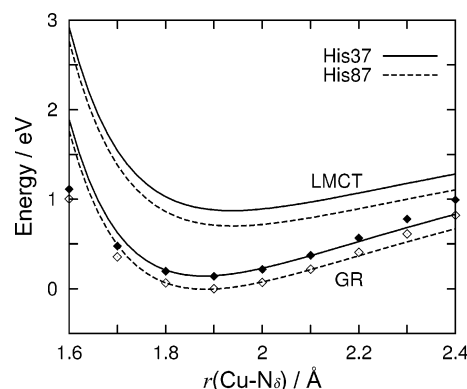


Figure 7. Potential energies along the Cu-N δ (His) distance, where one of the two His ligands, which is treated quantum mechanically, is shifted along the original Cu-N δ direction. The marked points are from the ROHF-MP2(ZAPT) calculations on the Cu(SCH₃)(Im)^{+/} (S(CH₃)₂)(Im) model in the ground state, and the solid and dashed curves are from the fitted potential functions. The curves in the LMCT state evaluated from the model potential functions are also included.

the His ligands, which modulates and controls the diabatic curve crossings in this way, is discussed next.

3.3. Ligand Force Fields for Cu-His and Cu-Met. *Cu-N(His) and Cu-S(Met) Distances.* Figure 7 shows the potential energy curves along the distance (R) between the Cu ion and the N δ atom of the His ligands. The ground (GR) state MP2 energies are fitted to a sum of the Coulomb and 12-6 Lennard-Jones (LJ) functions $V(R) = V_{\text{el}}(R) + V_{\text{LJ}}(R)$, the form commonly used in the standard force fields. The LJ parameters for the amino acids are taken from AMBER 94,⁴⁰ so that we only needed to determine the length (R_{Cu}^*) and energy (ϵ_{Cu}^*) parameters for the copper ion. The same combining rule as in AMBER is used, i.e., $R_{ij}^* = R_i^* + R_j^*$ and $\epsilon_{ij}^* = \sqrt{\epsilon_i^* \epsilon_j^*}$. Because the curves for His37 and His87 are very similar, we have taken the average of their optimized results, $R_{\text{Cu}}^* = 1.362$ Å and $\epsilon_{\text{Cu}}^* = 2.230 \times 10^{-3}$ kcal/mol. The lower curves labeled GR in Figure 7 are from this fitted function. The equilibrium Cu-N δ bond length from the calculation is 1.9 Å, being shorter than in the crystal structure, 2.0 Å, though within the resolution (1.9 Å) of the X-ray analysis.⁴

The upper curves in Figure 7, labeled LMCT, are computed from the same LJ parameters but different atomic charges of the fifth LMCT state. Reflecting the smaller copper positive charge (Table 3), the LMCT curves exhibit weaker bound potential with the minimum at longer distance. This feature is relevant to the discussion around Figure 6.

The corresponding procedure is repeated for the Cu-Met interaction. Here it was found necessary to introduce an additional function to the Coulomb and LJ potentials, for which we employed a Morse function $D(1 - e^{-a(R-R_e)})^2$. The result is displayed in Figure 8 with the optimized parameters $D = 23.76$ kcal/mol, $a = 0.9616$ Å⁻¹, and $R_e = 2.034$ Å. The calculation gives a notably shorter equilibrium Cu-S distance 2.4 Å than in the crystal structure, 2.9 Å, implying that the protein environment may be playing role. The potential in the LMCT state is also evaluated as in the Cu-His case. As seen, the LMCT curve is mostly parallel with the GR curve, reflecting the observation that the Coulomb interaction is less dominant in the Cu-Met potential, as has been discussed around Tables 1 and S2.

Cu-His Out-of-Plane Bend. Among the remaining coordinates for the metal-ligand structure, the out of plane bending angle between the copper ion and His ligands would be important because of the d- π interaction between the copper

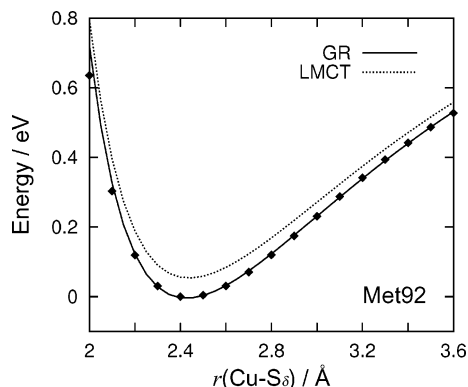


Figure 8. Similar to Figure 7 but for the Cu–Met interaction with the $\text{Cu}(\text{SCH}_3)(\text{S}(\text{CH}_3)_2)^+/(Im)_2$ model.

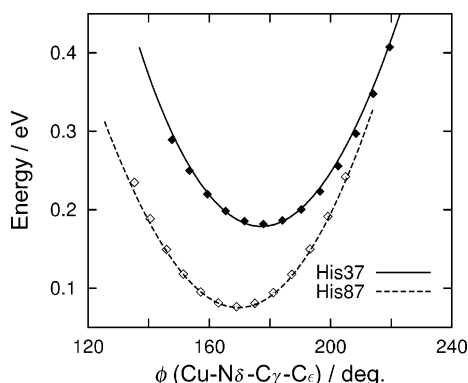


Figure 9. Similar to Figure 7 but now along the $\text{Cu-N}_\delta\text{-C}_\gamma\text{-C}_\epsilon$ torsional angle. The ligand structures are generated by bending the His ligand around an axis perpendicular to the Cu-N_δ axis and the normal axis of the plane formed by the $\text{N}_\delta\text{-C}_\gamma\text{-C}_\epsilon$ atoms.

d AOs and the imidazole π MOs. The MP2 energies along the torsional angle ϕ of the $\text{Cu-N}_\delta\text{-C}_\gamma\text{-C}_\epsilon$ sequence are fitted to a functional form

$$V(\phi) = V_b[1 + \cos(\phi - \phi_0)] \quad (6)$$

The results are shown in Figure 9. Again, the optimized V_b parameter was similar between His37 and His87, so we have taken their average, $V_b = 17.76$ kcal/mol. The phase angle ϕ_0 is -1.44° and -6.74° for His37 and His87, respectively. These small angles, which describe the nonplanarity, may be neglected in the molecular simulations. The potential curves in Figure 9 indeed show the importance of the d– π interaction.

Cys–Cu–His/Met Angles. We might expect no particular interactions of quantum mechanical origin, such as the d– π interaction just discussed, for the remaining intermolecular ligand structural coordinates. We have computed the KS-DFT energies of the entire $\text{Cu}(\text{SCH}_3)(Im)_2(\text{S}(\text{CH}_3)_2)^+$ model along the $\text{S}(\text{Cys})\text{-Cu-N}_\delta(\text{His})$ and $\text{S}(\text{Cys})\text{-Cu-S}(\text{Met})$ angles and compared them with the simple force field potentials of the Coulomb plus LJ functions that have been parametrized independently as above. The results are displayed in Figure 10. As expected, the agreement is not excellent, but of rather surprisingly good quality for the simple force field model to describe these weak interactions.

4. Concluding Remarks

The picture for the plastocyanin photodynamics and related phenomena emerging from the present calculations could be summarized as follows. After photoexcitation to the LMCT state, the $\text{Cu-S}(\text{Cys})$ bond elongates on the repulsive potential

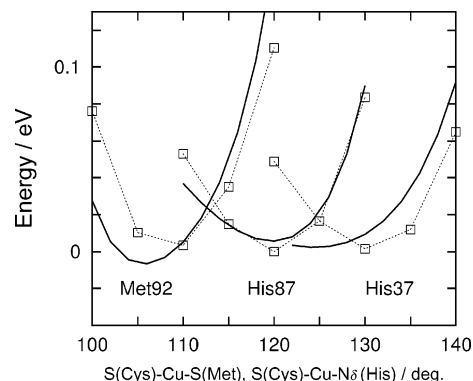


Figure 10. Potential energies along the $\text{S}(\text{Cys})\text{-Cu-S}(\text{Met})$ and $\text{S}(\text{Cys})\text{-Cu-N}_\delta(\text{His})$ angles. The marked points are from the KS-DFT/B3LYP calculations on the $\text{Cu}(\text{SCH}_3)^+(\text{S}(\text{CH}_3)_2)(Im)_2$ model. The dotted lines are to guide the eyes. The solid curves are from the force field model of Coulomb plus Lennard-Jones potentials, which has been developed independently of the KS-DFT results.

surface, which crosses with the d–d LF states at the $\text{Cu-S}(\text{Cys})$ distance of ~ 2.7 Å or longer. The surface crossing geometry is modulated by the fluctuation of the $\text{Cu-N}(\text{His})$ distance, such that the crossing may occur at a shorter $\text{Cu-S}(\text{Cys})$ distance when the $\text{Cu-N}(\text{His})$ distance is longer. This is explained by the different charge distributions and the resulting electrostatic interaction in these excited states. This suggests that the ligand vibrational motions of the Cu-His moiety represent a major reaction coordinate, in addition to the essential $\text{Cu-S}(\text{Cys})$ coordinate, in the nonradiative transitions from the LMCT to the d–d LF states. This transition pathway is in favor of the observation that the interaction between the Cu-Cys core and the His ligands becomes weaker in the LMCT state than in the ground state. On the other hand, the electrostatic perturbation from the Met ligand is rather minor compared to the His ligands, though it is possible that the Met ligand is involved via dispersion interaction due to the softness of the thioether group. The present MP2 calculations suggest a shorter equilibrium $\text{Cu-S}(\text{Met})$ distance ~ 2.4 Å than is found in the crystal, 2.94 Å, which implies that the protein strain and constraint may be playing some role, although its precise functional significance is yet unclear. Our preliminary MD simulations have suggested correlated motions of the Met92 ligand and the carbonyl group of proline36 adjacent to the His37 ligand. This issue will be further examined elsewhere.

We anticipate that the qualitative picture drawn here will mostly carry over after taking account of the perturbation from the protein environment. Nonetheless, it is obviously needed to proceed to the MD simulation analysis by using the potential functions developed here. In particular, it is intriguing to investigate what sort of protein collective motions may couple to the photodynamics mechanism, directly or indirectly via affecting the core ligand motions. Other issues of interest would be the quantum effects of the high-frequency nuclear vibrations,^{15,41} the renormalization of the reorganization energy by electronic polarization coupling,^{16,42,43} and the vibrational and electronic coherence^{8–10,17,18} in the ultrafast charge transfer dynamics. Works along this line are currently under way to be reported in forthcoming publications.

Acknowledgment. I acknowledge supports from The Royal Society (G503/22211) and EPSRC (GR/R60515).

Supporting Information Available: Tables of the full list of atomic charges, the electrostatic interactions between Cu-

Cys and His and Met ligands, the optimized parameters for the potential functions of eqs 4 and 5, and the optimized coordinates of hydrogens with the heavy atoms from the crystal structure. Pictures of the dominant active MOs and the CI coefficients from the MCSCF-ORMAS calculations. This material is available free of charge via the Internet at <http://pubs.acs.org>.

References and Notes

- (1) Gray, H. B.; Solomon, E. I. In *Copper Proteins*; Spiro, T. G., Ed.; Wiley: New York, 1981.
- (2) Sykes, A. G. *Adv. Inorg. Chem.* **1990**, *36*, 377.
- (3) Colman, P. M.; Freeman, H. C.; Guss, J. M.; Murata, M.; Norris, V. A.; Ramshaw, J. A. M.; Venkatappa, M. P. *Nature (London)* **1978**, *272*, 319.
- (4) Inoue, T.; Sugawara, H.; Hamanaka, S.; Tsukui, H.; Suzuki, E.; Kohzuma, T.; Kai, Y. *Biochemistry* **1999**, *38*, 6063.
- (5) For example, Sato, K.; Kohzuma, T.; Dennison, C. *J. Am. Chem. Soc.* **2003**, *125*, 2101 and references therein.
- (6) Solomon, E. I.; Baldwin, M. J.; Lowery, M. D. *Chem. Rev.* **1992**, *92*, 521.
- (7) Webb, M. A.; Loppnow, G. R. *J. Phys. Chem. B* **2002**, *106*, 2102.
- (8) Edington, M. D.; Diffey, W. M.; Doria, W. J.; Riter, R. E.; Beck, W. F. *Chem. Phys. Lett.* **1997**, *275*, 119.
- (9) Book, L. D.; Arnett, D. C.; Hu, H.; Scherer, N. F. *J. Phys. Chem. A* **1998**, *102*, 4350.
- (10) Nakashima, S.; Nagasawa, Y.; Seike, K.; Okada, T.; Sato, M.; Kohzuma, T. *Chem. Phys. Lett.* **2000**, *331*, 396.
- (11) Larsson, S.; Broo, A.; Sjölin, L. *J. Phys. Chem.* **1995**, *99*, 4860.
- (12) Ryde, U.; Olsson, M. H.; Pierloot, K.; Roos, B. O. *J. Mol. Biol.* **1996**, *261*, 586.
- (13) Pierloot, K.; Kerpel, J. O. A. D.; Ryde, U.; Roos, B. O. *J. Am. Chem. Soc.* **1997**, *119*, 218.
- (14) Pierloot, K.; Kerpel, J. O. A. D.; Ryde, U.; Olsson, M. H. M.; Roos, B. O. *J. Am. Chem. Soc.* **1998**, *120*, 13156.
- (15) Ando, K. *J. Chem. Phys.* **2001**, *114*, 9470.
- (16) Ando, K. *J. Chem. Phys.* **2001**, *115*, 5228.
- (17) Ando, K.; Santer, M. *J. Chem. Phys.* **2003**, *118*, 10399.
- (18) Ando, K.; Sumi, H. *J. Phys. Chem. B* **1998**, *102*, 10991.
- (19) We used a MacMolPlt software to generate Figure 1. Bode, B. M.; Gordon, M. S. *J. Mol. Graph. Modeling* **1999**, *16*, 133.
- (20) Stewart, J. J. P. *J. Comput. Chem.* **1989**, *10*, 209.
- (21) McWeeny, R.; Dierksen, G. *J. Chem. Phys.* **1963**, *49*, 4852.
- (22) Becke, A. D. *J. Chem. Phys.* **1993**, *98*, 5648.
- (23) Stephens, P. J.; Devlin, F. J.; Chabowski, C. F.; Frisch, M. J. *J. Phys. Chem.* **1994**, *98*, 11623.
- (24) Hertwig, R. H.; Koch, W. *Chem. Phys. Lett.* **1997**, *268*, 345.
- (25) Hehre, W. J.; Ditchfield, R.; Pople, J. A. *J. Chem. Phys.* **1972**, *56*, 2252.
- (26) Francl, M. M.; Pietro, W. J.; Hehre, W. J.; Binkley, J. S.; Gordon, M. S.; DeFrees, D. J.; Pople, J. A. *J. Chem. Phys.* **1982**, *77*, 3654.
- (27) Rassolov, V. A.; Pople, J. A.; Ratner, M. A.; Windus, T. L. *J. Chem. Phys.* **1998**, *109*, 1223.
- (28) In this work, we employed the geodesic method to generate the points on four layers of fused sphere van der Waals surfaces. Spackman, M. A. *J. Comput. Chem.* **1996**, *17*, 1.
- (29) Bayly, C. I.; Cieplak, P.; Cornell, W. D.; Kollman, P. A. *J. Phys. Chem.* **1993**, *97*, 10269.
- (30) Ivancic, J. *J. Chem. Phys.* **2003**, *119*, 9364.
- (31) Nakano, H. *J. Chem. Phys.* **1993**, *99*, 7983.
- (32) Roos, B. O. *Adv. Chem. Phys.* **1987**, *69*, 339.
- (33) Møller, C.; Plesset, M. S. *Phys. Rev.* **1934**, *45*, 618.
- (34) Lee, T. J.; Rendell, A. P.; Dyall, K. G.; Jayatilaka, D. *J. Chem. Phys.* **1994**, *100*, 7400.
- (35) Schmidt, M. W.; Baldrige, K. K.; Boatz, J. A.; Elbert, S. T.; Gordon, M. S.; Jensen, J. H.; Koseki, S.; Matsunaga, N.; Nguyen, K. A.; Su, S. J.; Windus, T. L.; Dupuis, M.; Montgomery, J. A. *J. Comput. Chem.* **1993**, *14*, 1347.
- (36) Mulliken, R. S. *J. Chem. Phys.* **1955**, *23*, 1833.
- (37) Reed, A. E.; Curtis, L. A.; Weinhold, F. *Chem. Rev.* **1988**, *88*, 899.
- (38) Here and hereafter, we might loosely use the terms His, Met, and Cys for the truncated amino acid models where confusion will not arise.
- (39) As expected, the calculations with shorter Cu–N distance (e.g., 1.8 Å) have resulted in a deformation of the potential curves in the opposite direction. However, we should be warned that the point charge approximation will become less adequate for the shorter metal–ligand distances. It thus remained an open question whether the ligand orbitals may be involved at the shorter distance to avail other channels for nonadiabatic transitions.
- (40) Cornell, W. D.; Cieplak, P.; Bayly, C. I.; Gould, I. R.; Merz, K. M.; Ferguson, D. M.; Spellmeyer, D. C.; Fox, T.; Caldwell, J. W.; Kollman, P. A. *J. Am. Chem. Soc.* **1995**, *117*, 5179.
- (41) Ando, K. *J. Chem. Phys.* **1997**, *106*, 116.
- (42) Kim, H. J.; Hynes, J. T. *J. Chem. Phys.* **1992**, *96*, 5088.
- (43) Marchi, M.; Gehlen, J. N.; Chandler, D.; Newton, M. D. *J. Am. Chem. Soc.* **1993**, *115*, 4178.